Solute transport in porous media studied by lattice Boltzmann simulations at pore scale and x-ray tomography experiments

Chunwei Zhang,* Tetsuya Suekane, Kosuke Minokawa, Yingxue Hu, and Anindityo Patmonoaji
Department of Mechanical Engineering, Tokyo Institute of Technology, 2-12-1-I6-33 Ookayama, Meguro-ku, Tokyo 152-8550, Japan

(Received 19 September 2019; published 26 December 2019)

With the aid of nondestructive microfocus x-ray computed tomography (CT), we performed three-dimensional (3D) tracer dispersion experiments on randomly unconsolidated packed beds. Plumes of nonreactive sodium iodide solution were point injected into a sodium chloride solvent as a tracer for the evaluation of the dispersion process. The asymptotic dispersion coefficient was obtainable within the experimental scale and was summarized over Péclet numbers from 11.7 to ∼860. Then, the lattice Boltzmann method and moment propagation method were used to elucidate the mechanisms embedded in the dispersion phenomenon. The methods were rigorously verified against the classical Taylor dispersion problem and extended to simulate fluid flow and tracer dispersion in high-resolution 3D digital porous structures from CT. The method of moments, Lagrangian velocity correction function, and dilution index were thoroughly analyzed to evaluate the dispersion behaviors. Numerical simulations revealed ballistic and superdiffusive regimes at the transient times, whereas asymptotic dispersion behaviors appear at longer characteristic times. Besides, the observed transient times unanimously persist over convective length scales of around 12 particles transversely and 16 particles longitudinally. The estimated dispersion coefficients from simulation are in consistence with the experimental result. Furthermore, the simulation also enabled the identification of regimes, including diffusive, power law, and mechanical dispersion. Thus, the proposed experimental and computational schemes are of practical means to study dispersion behaviors by direct pore scale imaging and modeling.

DOI: 10.1103/PhysRevE.100.063110

I. INTRODUCTION

Solute transport in porous media is a crucial mechanism in many engineering and industrial applications, such as electrolyte transport in cells and flow batteries [1], subsurface contaminant remediation [2], active phoretic swimmer transport through complex microstructures [3], and exploitation of carbonates [4]. However, dispersion behavior in hierarchical porous structures is immensely complex as the pore sizes and hydraulic conductivity are continuously evolving, generating velocity fluctuations and thus rendering production of well-defined temporal or spatial scale for asymptotic (Fickian) dispersion difficult [5]. Anomalous or preasymptotic behaviors characterized by a time-dependent dispersion coefficient may emerge in multiple experiments and simulations [6–8].

A tracer test is an efficient way of measuring the dispersion coefficient in the laboratory. The temporal extent of a tracer plume is often driven by convective forces stretching the plume, whereas the distribution of concentrations within the tracer plume is biasedly attenuated by diffusive or local dispersive processes [9]. Previous studies demonstrate that the transport of dissolved passive tracers in complex pore structures is characterized by transient intensive spreading at short timescales due to high bursts of fast flow and long-time predictable weak spreading or non-Fickian dispersion [10–12]. The three dispersion regimes identified include the following: (1) the ballistic dispersion that is characteristic of very short times, (2) the superdiffusive dispersion characteristic of intermediate times, and (3) the still superdiffusive dispersion or standard Fickian dispersion characteristic of long times. Nevertheless, predicting the scope of each regime remains a challenge.

Transient time was first defined by Taylor [13] as the time required for the radial variation of concentration to decay to $1/e$ of its initial value, and it is calculated through the expression $t_D = d^2/(3.8^2 D_m)$, where d is the pipe diameter and D_m is the molecular diffusion coefficient. Alternatively, transient time is the time needed for molecular diffusion to smooth out the infinitely growing convective longitudinal dispersion, also termed the velocity averaging process [14]. However, the transient time for solute transport in pore structures is often difficult to predict and might exhibit large variances. For example, long transient times and strong asymptotic dispersion coefficients are produced by increasing the heterogeneity of porous media, as discussed by Bruderer and Bernabé [14]. Fluid flow simulation in monodisperse sphere packing cylinders with different levels of heterogeneity yields similar results [15]. Altering the anisotropic permeability of porous media also changes the transient behavior. Maggiolo *et al.* [16] for example, reoriented fibers along streamlines of fibrous electrodes in redox flow batteries to minimize the drag force and improve the electrodes' dispersion coefficient.

*Present address: Department of Mechanical Engineering, Tokyo Institute of Technology, 2-12-1-I6-33 Ookayama, Meguro-ku, Tokyo 152-8550, Japan; zhang.c.aq@m.titech.ac.jp

Transient anomalous behavior, involving the superdiffusive and subdiffusive phenomena, might be explained by the pore-scale intermittent velocity structure [17] and temporal velocity fluctuations of the mean flow [18]. It can also be interpreted through including higher orders of moments, such as skewness and kurtosis [19]. In addition, the existence of vortices [20] in the flow field and intraparticle retention in stagnation zones [12] also contributes to the anomalous dispersion behavior. These cause pronounced contrast in local Péclet numbers, and hence non-Fickian phenomena, such as power-law residence time distributions and long tailing, are observed. The solid-liquid interface often involves a diffusive boundary layer [21], where tracer particles enter and exit mainly via diffusion because of extremely low velocity. Consequently, a long transient time is expected to reach the asymptotic dispersion region. Although dispersion behavior is well characterized and empirically correlated for inert particle packed beads [22,23] and partially for geologic rock samples, such as the Berea sandstones [24], the mechanisms underlying the specific transient anomalous behavior remain unclear. Therefore, experimental studies and pore-scale simulations are required to characterize and elucidate dispersion behaviors.

Recently, a direct observation of the three-dimensional (3D) dispersion in complex pore structures is made possible through nondestructive imaging technology, such as x-ray computed tomography (CT [6,25–29]). CT allows quantifying the dispersion phenomenon with enough spatial resolution, enabling the measurement of the strength of the dispersion process from reconstructed CT images. However, the available CT experimental results until now ahve been very limited since Boon *et al.* [25,29]. Boon *et al.* [25] developed a state-of-the-art NaI aqueous solution dispersion experimental system to study the transverse dispersion behavior in the cylindrical rock core, of centimeter scale, using a medical CT at resolutions of 1 mm. Boon *et al.* [29] also elaborately investigated the influence of the natural rock heterogeneity on the dispersion behaviors [29]. They rigorously justified that meandering, focusing, or splitting of the plume accounted for the non-Fickian spreading and mixing process. However, as macroscopic dispersion behaviors mainly emanate from microscale porous structures and complex velocity distributions, further experimental research is needed to clarify dispersion behaviors on much smaller scales. Hence, in this study, we focused on the point released NaI tracer plume dispersion behavior in packed particle beds of reduced size of tens of millimeters through an innovative micro-x-ray CT experiment system. The CT scanning image achieves a resolution of $\sim$100 μm.

On the other hand, pore-scale modeling is an important tool relating the macroscopic dispersion phenomenon with microscale flow and transport processes [30]. The most popular computational method is the lattice Boltzmann method (LBM [31,32]), which provides solutions to basic flow equations in complex porous structures at a manageable computational cost. Another method, the moment propagation method (MPM), was initially introduced to calculate the velocity autocorrelation function in the lattice gas model [33]. Its deliberate target was saving memory through propagation of a scalar field based on the distribution function f($\mathbf{v}$, $\mathbf{r}$, t). Later on, it was rigorously tested [34,35] and utilized to solve multiple convection, diffusion, and adsorption problems [36–38], particularly the transport of charged tracers in flow battery cells involving coupled effects of dispersion and electrostatic interactions. Thus, in this study, we extend the LBM and MPM method to simulate the dispersion process in the porous media.

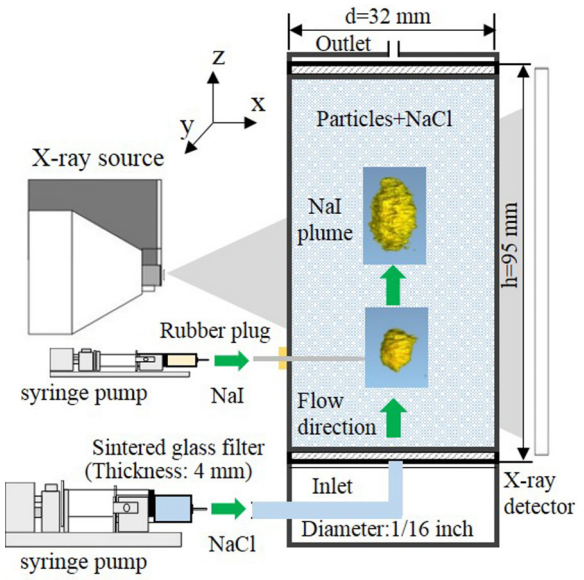

FIG. 1. Schematic view of the dispersion experiment apparatus with x-ray CT. The illustrated 3D configuration of the NaI tracer plume is visualized using the VGSTUDIO/MAX2.1 software.

In this work, we developed an innovative tracer dispersion experiment involving the point release of a sodium iodide (NaI) plume into a packed bed of melamine resin particles filled with sodium chloride (NaCl) solution with different stable flow rates. The experiments were conducted for Péclet numbers (Pe) from 11.7 to $\sim$860, with simultaneous visualization through microfocus x-ray CT. Then, pore-scale LBM and MPM simulations were utilized to solve the dispersion problem on the same porous media reconstructed from the CT images. The numerical schemes were verified against the classical Taylor dispersion in a fully developed Poiseuille flow. The dispersion coefficients estimated from the experiments and simulations were vastly compared with semianalytical data from previous studies. The transient dispersion behaviors were characterized from the simulation results and further assessed through the mean-square displacement, Lagrangian velocity correction function (LVCF), and dilution index.

II. EXPERIMENTAL METHODOLOGY

A. Experimental apparatus

A microfocus x-ray CT system (ScanXmate-RB090SS) was utilized to nondestructively measure the dispersion phenomenon, as shown in Fig. 1. Melamine resin particles (provided by Ube Sand Engineering Co., Ltd; XH series) were packed in an acrylic tube with an inner diameter of 32 mm and a height of 95 mm. The three mixed particle sizes utilized in this experiment are $d_p = 338$ μm (250−425 μm),

$d_p = 513\ \ \mu$m (425−600 μm), and $d_p = 780\,\mu$m (530−1030 μm). The x-ray scanner was operated at a stable voltage of 90 kV and current of 90 μA. Each scan comprised 625 continuous shots at a constant speed of 8.0 frames per second during the rotation of the image sensor through 360°, producing 992 fluoroscopic cross-sectional images. Therefore, the resulting CT image consisted of 992×992×992 pixels with a resolution of 103 μm/pixel. A single scanning time is around 80 s. Sintered glass filters were attached to the inlet and outlet of the packed tube to create a uniform and steady-state velocity field and prevent the leakage of experimental particles. A ring artifact reduction filter and noise removal filter surrounded the tube to eliminate the beam hardening effect [39]. A hole of 5 mm diameter was prepared for the NaI tracer injection at the lower 30-mm portion of the acrylic tube sealed with a silicone rubber septum (Shimadzu GLC Ltd.), pierced with an injection needle, and connected to a microsyringe pump (KD Scientific, KDS100) at the start of injection. The NaI tracer concentration is related with the brightness of the CT image through a calibration curve developed in advance, similar to that described in Wang *et al.* [40]. The initial concentration for the aqueous NaI solution was chosen as 10 wt %, because with this initial value a remarkable contrast between the NaI tracer and the surroundings was achievable throughout the experiment. An aqueous solution of 10 wt % NaCl was used as the default fluid, and the fluid pair was adjusted to the same density to eliminate buoyancy effects. The resulting density for the NaI and NaCl solution fluid pairs is 1.06 and 1.05 g/cm^3, respectively. The experiment was conducted at a room temperature of 25 °C. Moreover, as there is no chemical reaction and the total injection volume of NaI plume is relatively small, the perturbation of temperature during the experimental work can be neglected.

B. Experimental protocol

The acrylic tube was first filled with melamine resin particles and then completely saturated with the NaCl solution. This process was performed in a vacuum chamber to remove the undesirable gases. The porosities of the porous media created are directly determined through the mass change before and after saturation and showed nearly no reliance on the average particle diameters as presented in Table I. A 0.13-ml plume of NaI solution was then injected as a tracer at a constant flow rate of 2.5 ml/h via a syringe pump. This injection speed was chosen because higher injection speed will induce an undesirable transverse velocity so that a shift of the plume position may be encountered. This injection scheme ensured that the injection plume was as spherical as possible and prevented the plume from deviating from the cylinder central line. After injection, the fluid will accumulate and pass through the sintered glass filters both at the inlet and outlet of the acrylic tube to create a near-uniform flow field. This attempt can reduce the boundary effect. On the other hand, we placed the tracer injection point 30 mm away from the inlet to further avoid the inlet effect. Therefore, the effect of an additional pressure gradient can be deemed negligible. Afterwards, a total of 0.5 pore volume (PV) or 18 ml NaCl solution was injected upward from the bottom of the tube via a syringe pump and drained from outside through the top of the packed bed. The CT scan was performed for every 0.1 PV injection of the NaCl solution. The resulting CT scanning time intervals are 129.2, 64.6, 28.5, 8.6, and 4.3 s for NaCl solution flow rates of 100, 200, 500, 1500, and 3000 ml/h, respectively. Detailed experimental data are presented in Table I. The Péclet number (Pe) is defined as the ratio of the rate of advection and rate of diffusion. It is selected as a characteristic number, which is calculated as

TABLE I. Properties of porous media and range of Pe numbers in experiments.

d_p (μm)	ϕ	Q (ml/h)	u_{av} (m/s)	Pe
		100	6.91×10^{-5}	11.7
338		200	1.38×10^{-4}	23.4
	0.50	500	3.46×10^{-4}	58.4
(250–425)		1500	1.04×10^{-3}	175
		3000	2.07×10^{-3}	350
		100	7.05×10^{-5}	18.1
513		200	1.41×10^{-4}	36.2
	0.49	500	3.53×10^{-4}	90.4
(425–600)		1500	1.06×10^{-3}	271
		3000	2.12×10^{-3}	543
		100	7.35×10^{-5}	28.7
780		200	1.47×10^{-4}	57.4
	0.47	500	3.68×10^{-4}	143
(530–1030)		1500	1.10×10^{-3}	430
		3000	2.21×10^{-3}	860

$$\mathrm{Pe} = \frac{u_{\mathrm{av}}L}{D_m} = \frac{\frac{Q}{A}d_p}{\phi D_m}, \tag{1}$$

where Q (ml/h) is the main flow rate of the default NaCl solution, A (m^2) is the cross-sectional area (packing tube), d_p (μm) is the average particle diameter (melamine particles) selected as the characteristic length L, ϕ is the porosity, u_{av} (m/s) is the average fluid interstitial velocity, and D_m (m^2/s) is the molecular diffusion coefficient of iodide ions in water. In our study, D_m was chosen as a constant of 2×10^{-9} m^2/s, which corresponds to the self-diffusion coefficient for the infinite dilation of NaI in water [41].

III. NUMERICAL METHODOLOGY

Recently, the LBM has been increasingly used to solve fluid dynamics problems and is second order in accuracy to recover Navier-Stokes equations [32,42,43]. The use of the LBM is advantageous in simulating porous media flows with complex geometrical structures and tortuous curvatures [32] because of the computational efficiency and physical accuracy involved. Hence, in this study, we employ the LBM with He's forcing scheme [44] to simulate fluid flow under the experimental condition. The implementation of the equivalent body force and periodical boundary conditions allowed the reproduction of the pressure gradient (or momentum input) and the resulting flow field. After stabilizing the flow field through LBM iterations, the MPM was adopted to simulate advection and diffusion in the porous medium. The details of the numerical scheme are provided below.

A. LBM

In this study, the D3Q19 LBM with He's forcing scheme [44] is implemented to simulate the equivalent pressure-driven flow. A statistical description of the lattice Boltzmann distribution function $\mathrm{f}(\mathbf{v}, \mathbf{r}, \mathrm{t})$ is expressed as follows:

$$d\mathrm{f}/d\mathrm{t} = \mathbf{v}\partial\mathrm{f}/\partial\mathbf{r} + \mathbf{a}\,\partial\mathrm{f}/\partial\mathbf{v} + \partial\mathrm{f}/\partial\mathrm{t} = -(\mathrm{f} - \mathrm{f}^{\mathrm{eq}})/\tau_{\mathrm{f}}, \quad (2)$$

where $\mathrm{f}(\mathbf{v}, \mathbf{r}, \mathrm{t})$ denotes the probability of having particles at time t positioned between $\mathbf{r}$ and $\mathbf{r} + d\mathbf{r}$ with velocities between $\mathbf{v}$ and $\mathbf{v}+d\mathbf{v}$ and $\mathbf{v}$ is the lattice velocity and can be discretized into a set of lattice velocities $\mathbf{e_i}$ along the allowable ith direction in the 3D Cartesian coordinate system as

$$\mathbf{v} = \{\mathbf{e}_0, \ldots, \mathbf{e_i}, \mathbf{e}_{18}\} = \begin{cases} (0,0,0)c, & i = 0 \\ (\pm1,0,0)c,\ (0,\pm1,0)c,\ (0,0,\pm1)c, & i = 1-6 \\ (\pm1,\pm1,0)c, \quad (\pm1,0,\pm1)c, \quad (0,\pm1,\pm1)c, & i = 7-18 \end{cases}. \quad (3)$$

The right side of Eq. (2) represents the collision operator with Bhatnagar-Gross-Krook-Welander (BGKW) approximation, where τ_{f} is the relaxation factor associated with the fluid viscosity, and $v = c_s^2(\tau_{\mathrm{f}} - 0.5)$; c_s is the lattice sound speed, and $c_s^2 = \frac{c^2}{3} = RT$; f^{eq} is the equilibrium Maxwell-Boltzmann distribution function. In the 3D Cartesian coordinate system, f^{eq} can be discretized as

$$f_i^{\mathrm{eq}} = \left\{ \begin{array}{ll} \frac{\rho}{3} - \frac{1}{2}\rho\cdot\mathbf{u}^2, & i = 0, \\ w_i \left[\begin{array}{c} \rho + \rho(\mathbf{e_i}\cdot\boldsymbol{u}) \\ +\frac{9}{2}\rho(\mathbf{e_i}\cdot\mathbf{u})^2 \\ -\frac{3}{2}\rho\cdot\mathbf{u}^2 \end{array} \right], & i = 1{-}18 \end{array} \right\}, \quad (4)$$

where ρ is the fluid density, $\mathbf{u}$ is the macroscopic fluid velocity, and w_i is the weighing factor chosen to ensure an isotopic tensorial structure up to the fourth order [45].

$$w_0 = \tfrac{1}{3}, \quad w_{1\sim6} = \tfrac{1}{18}, \quad w_{7\sim18} = \tfrac{1}{36}\ (i = 0,\ 1, \ldots,\ 18). \quad (5)$$

The left part of Eq. (2) represents the advection (streaming) term with a source term (external force), and $\boldsymbol{a} = \mathbf{F}/\rho$ is the acceleration due to the equivalent-volume force $\mathbf{F}$, which is further expressed as

$$\boldsymbol{a}\frac{\partial f}{\partial \mathbf{e_i}} \approx \frac{\mathbf{F}}{\rho}\frac{\partial f_i^{\mathrm{eq}}}{\partial \mathbf{e_i}} = -\frac{(\mathbf{e_i} - \boldsymbol{u})\cdot\mathbf{F}}{\rho c_s^2} f_i^{\mathrm{eq}} \quad (6)$$

The source term is designed to induce a momentum input on the fluid system while the fluid density remains unchanged [32] as expressed below:

$$\frac{\partial \rho}{\partial t} \equiv \sum_i \frac{(\mathbf{e_i} - \mathbf{u})\cdot\mathbf{F}}{\rho c_s^2} f_i^{\mathrm{eq}} = 0. \quad (7)$$

$$\frac{\partial \rho \boldsymbol{u}}{\partial t} \equiv \sum_{\boldsymbol{i}} \boldsymbol{e_i}\frac{(\boldsymbol{e_i} - \boldsymbol{u})\cdot\boldsymbol{F}}{\rho c_s^2} f_i^{\mathrm{eq}} = \mathbf{F}. \quad (8)$$

In conventional computational fluid dynamics, the pressure difference is dependent on the attendant density changes with $\delta P = \delta\rho c_s^2$, such that small changes in pressure induce violations of the incompressibility conditions. Numerically, it is reasonable to maintain a constant pressure gradient (momentum input) in the flow system by introducing a constant body force.

Therefore, the discrete transport equation with the external forces [46,47] can be written as

$$\frac{\partial f_i}{\partial t} + \mathbf{e_i}\frac{\partial f_i}{\partial \mathbf{r}} = \frac{1}{\tau_f}\left[f_i^{(\mathrm{eq})}(\mathbf{r}, t) - f_i(\mathbf{r}, t)\right] + \frac{(\mathbf{e_i} - \mathbf{u})\cdot\mathbf{F}}{\rho c_s^2} f_i^{\mathrm{eq}}. \quad (9)$$

The assumption that τ_f is constant over a step yields an artificial viscosity that is adsorbed into the real viscosity of fluids. However, as addressed by He *et al.* [44], the trapezoidal rule is required to achieve a second-order accuracy in time. To eliminate the implicitness of Eq. (9), the rearranged density distribution function $h_i(\mathbf{r}, t)$ is introduced as

$$h_i(\mathbf{r}, t) = f_i(\mathbf{r}, t) - \Delta t\frac{(\mathbf{e_i} - \mathbf{u})\cdot\mathbf{F}}{2\rho c_s^2} f_i^{\mathrm{eq}}(\mathbf{r}, t). \quad (10)$$

Therefore, the LBM equation with He's forcing scheme can be written as

$$h_i(\mathbf{r} + \mathbf{e_i}\Delta t,\ t + \Delta t) - h_i(\mathbf{r}, t) = \frac{\Delta t}{\tau_{\mathrm{f}}}\left[f_i^{\mathrm{eq}} - h_i(\mathbf{r}, t)\right] + \left(1 - \frac{1}{2\tau_{\mathrm{f}}}\right)\Delta t\frac{(\mathbf{e_i} - \mathbf{u})\cdot\mathbf{F}}{\rho c_s^2} f_i^{\mathrm{eq}}, \quad (11)$$

and the macroscopic fluid density ρ and fluid velocity $\mathbf{u}$ are calculated as

$$\rho = \sum h_i, \quad \rho\mathbf{u} = \sum h_i\mathbf{e_i} + \frac{1}{2}\mathbf{F}\Delta t = \sum f_i^{\mathrm{eq}}\mathbf{e_i}. \quad (12)$$

The above LBM equations are transformed to second order for accuracy to the standard Navier-Stokes equations through the Chapman-Enskog expansion, which is given as

$$\frac{\partial \mathbf{u}}{\partial t} + (\mathbf{u}\cdot\nabla)\mathbf{u} = \nu\nabla^2\mathbf{u} - \frac{\nabla P}{\rho} + \frac{\mathbf{F}}{\rho}. \quad (13)$$

B. MPM

Instead of solving the classical advection and diffusion equation, the MPM evolves the scalar quantity with an ensemble of kinetic equations [35]. The resulting statistical errors in the autocorrelation function are therefore largely reduced. The moment propagation equation expands the quantity of scalar $C_i(\boldsymbol{r}, t)$ through a discrete equation, and summarizing $C_i(\boldsymbol{r}, t)$ along all directions yields the concentration profile of the tracer in the flow field. By employing the LBM scheme with He's forcing scheme, the equilibrium function $f_i^{\mathrm{eq}}(\mathbf{r}, t)$ is only a function of the fluid velocity; therefore we can use

TABLE II. Simulation schemes.

d_p (l.u.)	g (l.u.)	U_{av} (l.u.)	Pe	Re	K_m (l.u.)
	6.08×10^{-5}	1.95×10^{-4}	11.7	0.03	0.534
	1.22×10^{-4}	3.90×10^{-4}	23.4	0.05	0.533
20 (0.26)	3.05×10^{-4}	9.75×10^{-4}	58.4	0.12	0.533
(14.8–25.2)	9.12×10^{-4}	2.93×10^{-3}	175	0.34	0.535
	1.83×10^{-3}	5.83×10^{-3}	350	0.75	0.532
	1.65×10^{-4}	3.01×10^{-4}	18.1	0.04	0.304
20 (0.22)	3.29×10^{-4}	6.02×10^{-4}	36.2	0.07	0.305
(16.6–24.4)	8.30×10^{-4}	1.51×10^{-3}	90.4	0.19	0.302
	2.48×10^{-3}	4.52×10^{-3}	271	0.54	0.304
	4.95×10^{-3}	9.05×10^{-3}	543	1.09	0.305
	3.86×10^{-4}	4.78×10^{-4}	28.7	0.06	0.206
	7.80×10^{-4}	9.56×10^{-4}	57.4	0.12	0.204
20 (0.32)	1.94×10^{-3}	2.39×10^{-3}	143	0.29	0.205
(13.6–26.4	5.76×10^{-3}	7.15×10^{-3}	430	0.86	0.207
	1.16×10^{-2}	1.44×10^{-2}	860	1.72	0.206

the following equation to evolve the scalar quantity $C_i(\mathbf{r},t)$ [33,35].

$$C_i(\mathbf{r},t+\Delta t)=\left[\frac{f_i^{\mathrm{eq}}(\mathbf{r},t+\Delta t)}{\rho(\mathbf{r},t)}-w_i\Delta\right]C_i(\mathbf{r}-\mathbf{e_i}\Delta t,t)+\Delta C_i(\mathbf{r},t). \tag{14}$$

The first term on the right of the equation accounts for tracer particles leaving location $\mathbf{r}$ in the $\mathbf{e_i}$ direction. The second term denotes the fraction of particles remaining at the node $\mathbf{r}$ through one iteration time step Δt.

The recovered convection and diffusion equation is given as

$$\partial_t C=-\mathbf{u}\partial_r C+\frac{c_s^2}{2}(1-\Delta)\Delta t\partial_r^2 C+o(\Delta t\partial_t C)+o\left(\Delta\mathbf{r}^2\partial_r^2 C\right). \tag{15}$$

Assuming that the flow velocity is extremely low and diffusion is isotropic in all possible directions, the diffusion coefficient is approximated using a nondimensional parameter Δ as $D=\frac{c_s^2}{2}(1-\Delta)\Delta t$ through the Chapman-Enskog expansion. The diffusion coefficient can also be written in terms of the grid Péclet number ($\mathrm{Pe}_{\Delta x}=u\Delta x/D$), Courant number (Cr) as follows [48]:

$$D=\mathrm{Cr}\Delta x^2/(\Delta t\mathrm{Pe}_{\Delta x}). \tag{16}$$

A limitation of the $\mathrm{Pe}_{\Delta x}$ is required for the non-negativity of the concentration field and numerical stability [34,35,48]. As suggested by Yu *et al.* [35], the MPM is more suitable for simulation in regions with low velocity and high concentration gradient, and the maximum $\mathrm{Pe}_{\Delta x}$ for a stable and a reasonable result can reach as high as 100. In our simulation work, this condition is satisfied as the largest simulated $\mathrm{Pe}_{\Delta x}$ is around 43 (see Table II, $\mathrm{Pe}_{\Delta x\mathrm{max}}=860/20$). In addition, an appropriate choice of *Cr* number, following the Courant-Friedrichs-Lewy law [49,50], given as below:

$$\mathrm{Cr}=u\Delta t/\Delta x\ll 1, \tag{17}$$

is necessary for the numerical diffusion reduction and convergence while solving the partial differential equations, even though this condition is robust in the present study with fluid velocity u on the order of 10^{-5}–$\sim10^{-3}$ m/s. However, it does not mean that the smaller Cr number the better, as the smaller Cr value will elongate the total simulation time. In our simulation, the Cr number is fixed at ~0.01 by elaborately determining the iteration time step Δt for the given diffusion coefficient D.

C. Model verification

To validate the numerical scheme, the LBM with He's forcing scheme and MPM are employed to simulate the Taylor-Aris dispersion [13] in a fully developed Hagen-Poiseuille laminar tube flow. The tube, which is 40 lattices in diameter and 240 lattices in length, is initially filled with water of density equal to 1 l.u. and viscosity of $\upsilon=\frac{1}{6}$ l.u. "l.u." represents the lattice Boltzmann unit of the corresponding physical properties. The flow was driven by a constant body force $g=1\times10^{-6}$ l.u. along the y direction to generate the equivalent pressure gradient. The periodical boundary condition is applied at the inlet and outlet, whereas the halfway bounce-back scheme is applied to the walls. Through simulation, the resulting velocity field exhibits a parabolic distribution (data not shown here) along the transverse direction with $U=\frac{g}{4\upsilon}(R^2-r^2)$ and shows an average of $\bar{U}=2.95\times10^{-4}$ l.u. that is very close to the analytical solution $\bar{U}=\frac{g}{8\upsilon}R^2=3\times10^{-4}$ l.u., where R and r represent the tube radius and distance to the tube center, respectively. After stabilization of the flow field, a tracer plume with a diameter of ten lattices was point injected into the upstream center line of the tube. The constant diffusion coefficient was set as $D_m=3.33\times10^{-4}$ l.u. The analytical solution of Eq. (15) for instantaneous point release [51,52] is given as

$$C_x(t)=\frac{M/A}{\sqrt{4\pi D_T t}}\exp\left(-\frac{x^2}{4D_T t}\right), \tag{18}$$

$$C_y(t)=\frac{M/A}{\sqrt{4\pi D_L t}}\exp\left[-\frac{(y-\bar{U}t)^2}{4D_L t}\right], \tag{19}$$

where D_T and D_L are the directional dispersion coefficients, M is the injected tracer mass, and A is the cross-sectional area of the tube. The evolution of the average concentration profile over the x and z planes along the y direction is depicted in Fig. 2. The deformation of the plume after injection is illustrated in the insets from (a) to (f), with a parabolic shape resembling the velocity distribution profile. A diffusion boundary layer emerged near the solid wall of the tube at a later time of dispersion. The transverse variation in concentrations is created by the shear flow tilting and stretching of the plume, while the same quantity is also destroyed by transverse molecular diffusion [53]. At a later time, the transverse concentration differences are negligible compared with the axial counterparts.

The evolution of the relative dispersion coefficient $D_{L/T}/D_m$ is displayed in Fig. 3. The dispersion coefficient was calculated in accordance with Brenner's method of the second

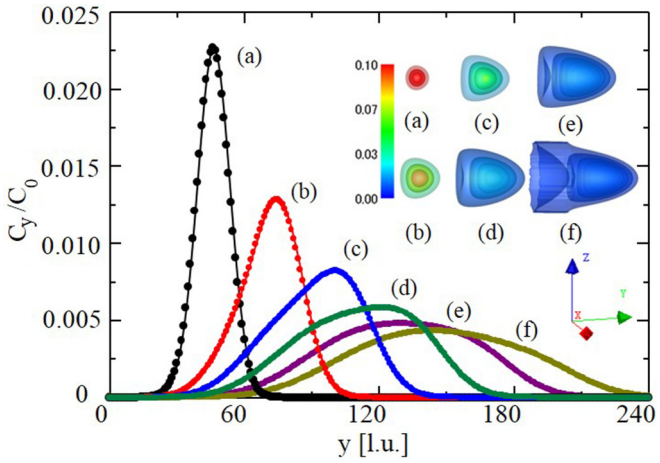

FIG. 2. Concentration profile along the flow direction averaged at the y plane of the tube. The isovolume plots (a)–(f) illustrate the concentration profile at times $t = 60\,000$, $t = 120\,000$, $t = 180\,000$, $t = 240\,000$, $t = 300,000$, and $t = 360\,000$ l.u., respectively. The tracer dispersion after point (e) has passed the transient period and becomes stabilized.

central moment [54], which is given as

$$\bar{x} = \frac{\sum_i C_i x_i}{C_0}, \quad \bar{y} = \frac{\sum_j C_j y_j}{C_0}, \tag{20}$$

$$\sigma_T^2 = \frac{\sum_i \{C_i (x_i - \bar{x})^2\}}{C}, \quad \sigma_L^2 = \frac{\sum_j \{C_j (y_i - \bar{y})^2\}}{C}, \tag{21}$$

$$D_{T,L} = \frac{1}{2} \frac{d\sigma_{T,L}^2}{dt}, \tag{22}$$

where C_i and C_j are the sums of the tracer concentration in the i and j planes where the tracer particles reside; C_0 is the sum of the concentrations over the entire domain; $\bar{x}$ and $\bar{y}$ are the average positions of the plume in the x and y directions; and

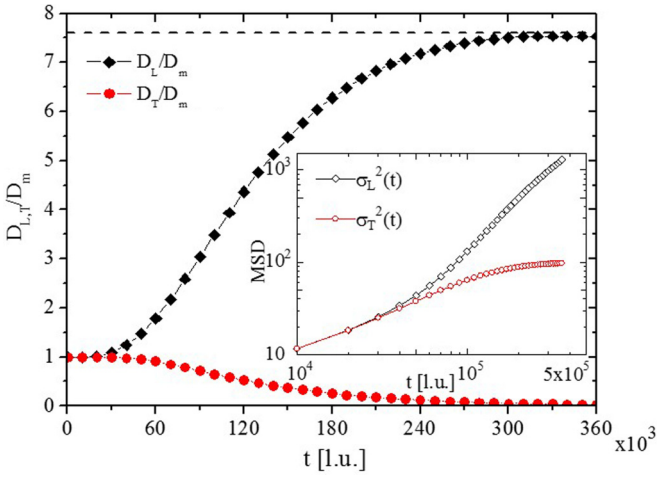

FIG. 3. Evolution of the nondimensional dispersion coefficients after injection of an immiscible passive tracer plume with a diameter of ten lattices into a fully developed pressure-driven Hagen-Poiseuille tube flow with a pipe diameter of 40 lattices. The inset depicts the temporal evolution of the MSD.

σ_T^2 and σ_L^2 are the mean-square displacements (MSDs) in the transverse and longitudinal directions and are related to the dispersion coefficients in Eq. (22).

The dispersion coefficients in both the longitudinal and transverse directions start from the molecular diffusion coefficient. However, while the dispersion in the longitudinal direction increases because of the shear force, the dispersion in the transverse direction is abated by the confining walls and boundary-layer effects. Beyond the 30 000th time step, the Taylor dispersion is fully developed with a constant relative dispersion coefficient of 7.54 l.u. in the longitudinal direction but of nearly zero in the transverse direction**.** The dashed line denotes the relative longitudinal diffusion coefficient D_L/D_m computed from the classical analytical equation as $\frac{D_{\text{eff}}}{D_m} = (1 + \frac{1}{192}\text{Pe}^2) = 7.61$ [13], where $\text{Pe} = \frac{\bar{U}d}{D_m} = 35.44$ in our simulation. The transient time for the stable Taylor dispersion happens to be close to Taylor's expression with $t_D = \frac{d^2}{3.8^2 D_m} = 332\,000$ l.u., which also approximates the time required for the tracer in the tube central line to pass the shear field and diffuse to the boundary. Assuming that the tube diameter represents the pore diameter, the tracer particle travels at least six pore diameters to stabilize.

IV. SIMULATION SCHEME

Based on the reconstruction from the experimental porous media CT images, a cube with dimensions of 120 × 400 × 120 voxels was chosen as the simulation domain as illustrated in Fig. 4(a). The resolution of the scanned porous media is set to adjust the average particle size d_p to 20 lattice units, resulting in a resolution of $L = 16.9$, 25.6, and 39 μm/voxels for averaged particle size of 338, 513, and 780 μm. Hence, approximately 700 melamine resin particles were included in each case. The pore size CDF plots are displayed in Figs. 4(c) and 4(d), with similar patterns despite differences in the particle diameter ranges. Spatially periodical boundary conditions with half-way bounce-back schemes are applied at all boundaries, whereas an equivalent pressure gradient ($\partial P/\partial y = \rho g$) is exerted in the longitudinal (y) direction. Details of all experimental settings are presented in Table II. The permeability of the porous medium is calculated from the classical Darcy law given as $K_m = \mu U_{\text{av}}/\nabla P = \nu U_{\text{av}}/g$, where U_{av} is the mean flow interstitial velocity averaged over all fluid points. The statistical probability density functions of the interstitial velocity in the transverse and longitudinal directions are displayed in Fig. 4(b). Gaussian distribution with zero mean is discovered for the PDF of the transverse velocity. The nonshift of transverse velocity field implies that no additional pressure gradient is imposed transversely, and Gaussian distribution indicates the simulation domain is sufficiently homogeneous to be representative of the intrinsic porous structures, as the transverse velocity is mainly originated from the fluid flow bypassing the particles. Furthermore, the calculated permeability values for the three porous media are 1.52×10^{-10}, 2.00×10^{-10}, and 3.13×10^{-10} m^2. The permeability values are consistent with the results from the water flooding experiments of similar porous media by Nakanishi *et al.* [55], which yielded values of 1.30×10^{-10}, 1.90×10^{-10}, and 2.63×10^{-10} m^2. This finding indicates that the simulation

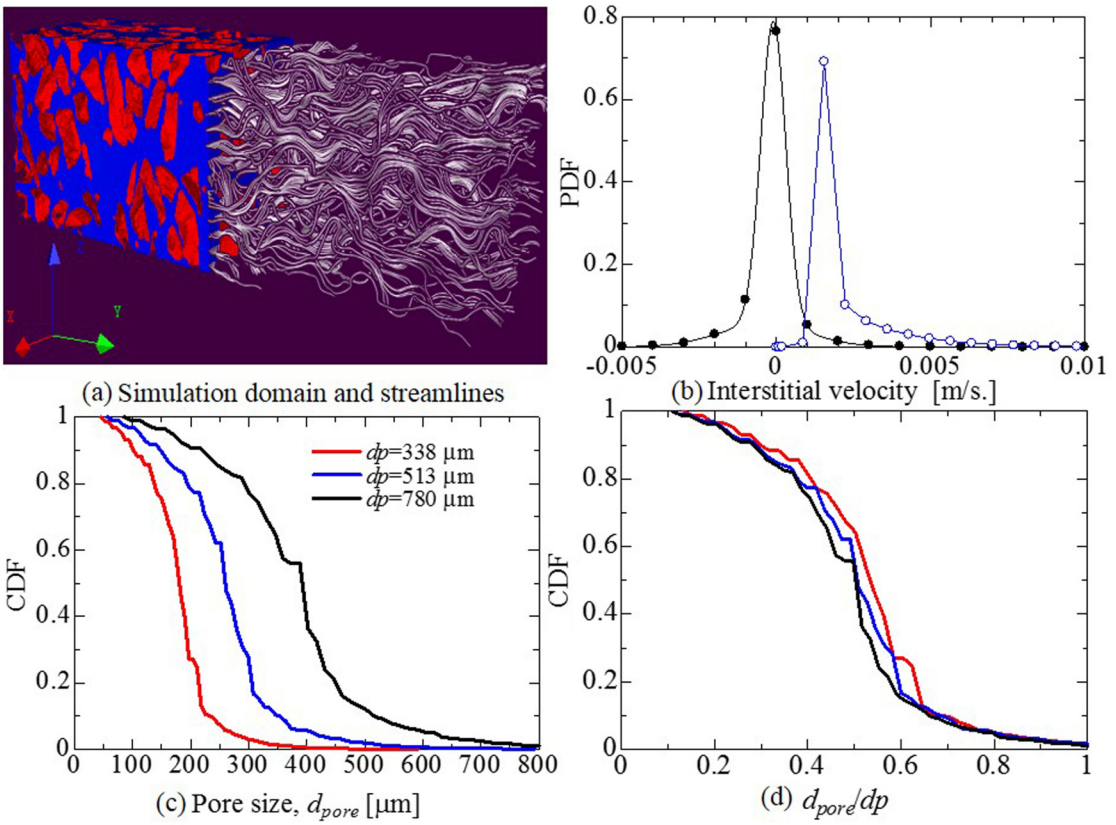

FIG. 4. Porous media showing pore size distributions and steady-state flow fields. (a) The left half represents the melamine resin particles (red represents particles and blue denotes pore spaces), and the right half represents the streamlines at $\mathrm{Pe} = 350.4$ and $d_p = 338\ \mu$m. (b) Probability density function of the interstitial velocity (PDF). (c) Cumulative density function (CDF) for the pore size distribution, representing the probability of the occurrence of a pore size larger than d_{pore}. (d) CDF plotted as a function of the rescaled particle diameter.

domain is representative of the intrinsic pore structures. Therefore, simulations in the subdomain of the porous structure can be linked with the experimental results.

To match the LBM parameters with the real physical values (marked with a superscript *), we choose the following common dimensional equations: $l^* = l_0 l$, $\nu^* = \nu_0 \nu$, $\upsilon^* = \upsilon_0 l_0 \nu$. Parameters with a superscript 0 are the characteristic scaling parameters. The characteristic scaling length l_0 is chosen as one pixel resolution L for the CT scan. The viscosity of the brine was set to a constant value of $\nu = (2\tau - 1)/6 = 1/6$ l.u., corresponding to the physical quantity of $\nu^* = 10^{-6}\ \mathrm{m}^2/\mathrm{s}$. Similarly, the molecular diffusion coefficient was set to $D_m = 3.33 \times 10^{-4}$ l.u. to match the physical value of $D_m^* = 2 \times 10^{-9}\ \mathrm{m}^2/\mathrm{s}$.

V. RESULTS AND DISCUSSION

A. Experimental results

The temporal visualization of the injected tracer plume concentration distribution is displayed in Fig. 5. It was obtained by transforming the local CT brightness values to local concentrations through the calibration curves. For the detailed image processing and noise reduction procedures refer to the work of Sin *et al.* [39], involving the removal of undesirable local spot brightness through additional filters and image subtraction. The accuracy of the experiment is validated by keeping the variation of the tracer amount within 5% for each scan. The concentration of the NaI solution at the initial condition was nearly 10 wt %, and it decayed to approximately 2–3 wt % after the injection of 0.5 PV (18.0 ml)

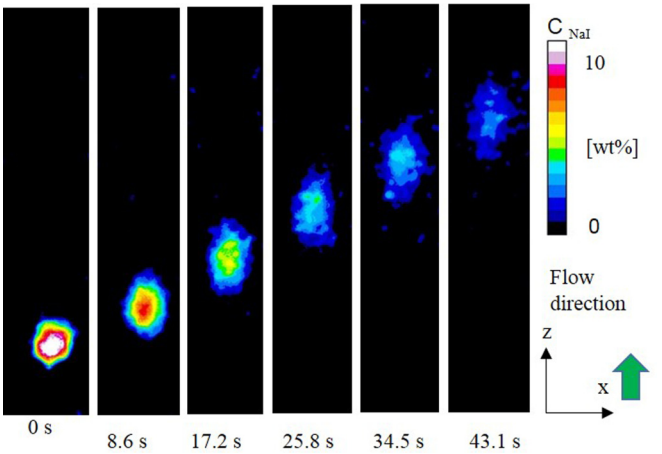

FIG. 5. Visualization of the local NaI concentration distributions over time projected in the xz plane. The NaCl solution flow is in the z direction. The concentration of the NaI solution at the initial condition was nearly 10 wt %, and it decayed to approximately 2–3 wt % after injection of 0.5 PV NaCl solution ($\mathrm{Pe} = 350.4$, $d_p = 338\ \mu$m).

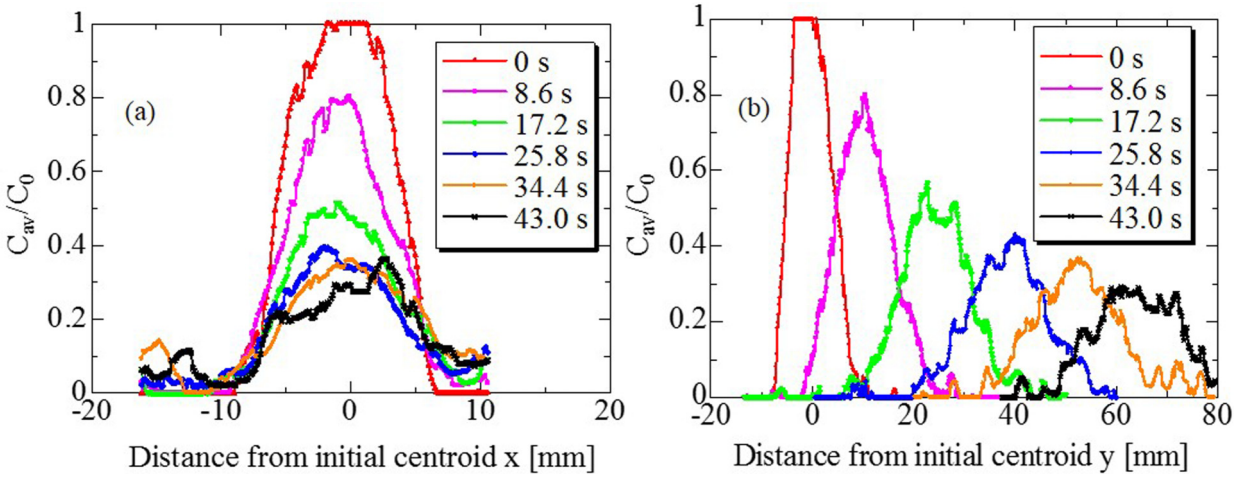

FIG. 6. Temporal evolution of the transverse (a) and longitudinal (b) tracer plume configurations projected in the x and y planes (Pe $= 350.4$, $d_p = 338\,\mu$m).

NaCl solution. The centroid of the plume gravity in the longitudinal and transverse directions was estimated based on each image and used as the reference for the determination of the MSD specified in Eqs. (20)–(22). The position of the centroid in the longitudinal direction linearly proceeded with time as a result of the strong convective effects at the experimental condition. However, the transverse centroid position remained almost unchanged, highlighting the homogeneous nature of the porous media.

To better interpret the decay in the tracer concentration, we projected the temporal evolution of the plume distribution in the transverse and longitudinal directions (Fig. 6). The maximum tracer concentration resides in the centroid of the tracer plume, and it exponentially decays with increasing time. Assuming Fickian dispersion, the decay of the maximum concentration in either direction will analytically follow $C_{\max}/C_0 \sim t^{-0.5}$ [see Eqs. (18) and (19)]. In our experiment, the power law is estimated as -0.52 and -0.61 for the transverse and longitudinal directions, respectively. Although the local fluctuations of the concentration fields blur the anisotropic Gaussian distribution of the tracer cloud, Fick's law of diffusion is a reasonable approximation for the description of the embedded dispersion behaviors.

To facilitate the above analysis, Brenner's method of the second central moment [54] was utilized to calculate the dispersion coefficients. The temporal evolution of the longitudinal and transverse spatial variances is shown in Fig. 7. Linear growth of the MSD with time in the longitudinal and transverse directions is observed for all experiments, unambiguously suggesting the attainment of the asymptotic dispersion region. Nevertheless, the superimposed ballistic diffusion growth of the spatial variance was lacking for all experiments, indicating failure to capture the transition from the preasymptotic dispersion behaviors during the experimental time and spatial scales. Pore scale simulations are required to clarify the scales for the initial transient dispersion behaviors. The dispersion coefficient estimated for each experiment is presented in Sec. V E to make comparisons with the LBM simulation results against a wide range of Pe.

B. Pore-scale dispersion simulation results

Figure 8 shows the temporal evolution of the tracer plumes from the simulation. The concentration of the NaI solution quickly decays from the plume centroid to the outer surface at the preasymptotic times, and consequently the initial distribution effect is barely evident after just 0.714 s. Thereafter, the symmetric structure of the pluglike tracer cloud is dissociated as the particles preferentially migrate through pore throats with presumably low drag forces and high burst of velocities. Due to the existence of large shear forces around the obstacle surfaces where large velocity gradients occur, the tracer particles accumulate in the vicinity of the obstacles to form fingerlike structures. These structures further obstruct dispersion in the antistreamwise direction and hence amplify dispersion along the streamlines. This shear-induced dispersion phenomenon likely explains the enhanced dispersion behaviors in the porous media [56]. However, after the plume cloud samples enough pore throats over time ($t > 2.865$ s), the concentration profile of the plume is largely smoothed, suggesting the attainment of the preasymptotic mixing state. To compare with the experimental results, the synchronized configuration of the tracer concentration is plotted in Fig. 9.

At early time steps, the concentration distribution is characterized by multiple peaks for the transverse and longitudinal directions. However, the distributions turned more and more Gaussian shaped at later times, implying the emergence of the transition to Fickian dispersion within the simulation temporal scale. At a later time of the simulation, although the tracer particles exit and reenter the porous media (gray line in Fig. 9) due to the implementation of the periodical boundary conditions, nearly no overlap is visible between the tracer particles, suggesting the adequacy of the computational geometrical length scale. The fact that the maximum tracer concentration decays faster in the longitudinal direction indicates a stronger dispersivity in the longitudinal direction than the transverse direction. In particular, some isolated tracer plumes are visible near the initial centroid [see Fig. 8(g) and the red line in Fig. 9]. Similar phenomena are observed in our experiment (shown in Fig. 5), where the segregated tracer

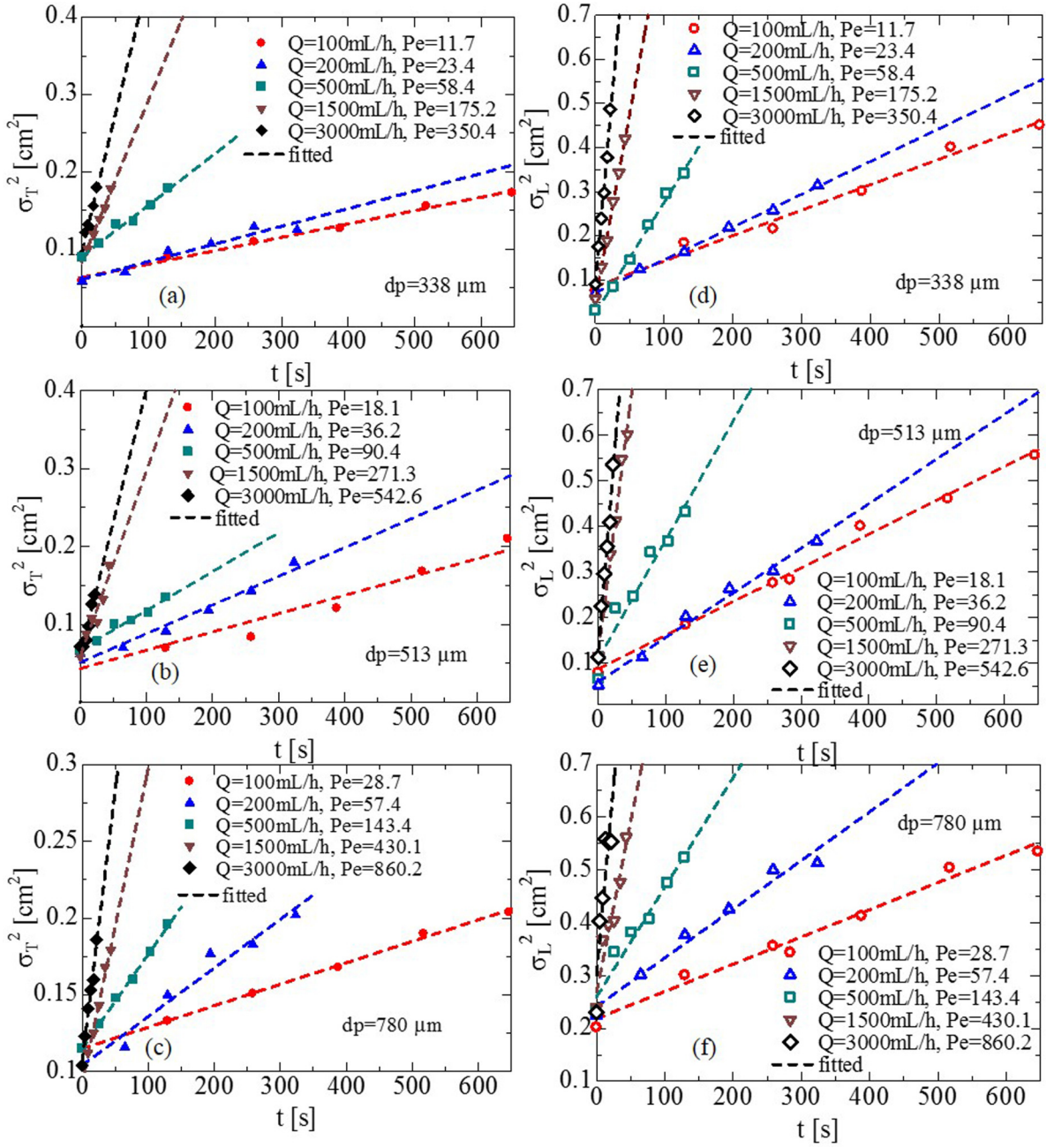

FIG. 7. Temporal evolution of the longitudinal and transverse spatial variances. The time intervals are 129.2, 64.6, 28.5, 8.6, and 4.3 s for volume flow rates of $Q = 100$, 200, 500, 1500, and 3000 ml/h, respectively; six continuous x-ray scans were taken for each experiment. The dashed lines denote the linearly fitted lines of the data acquired at each time step, with half of the slope value representing the dispersion coefficients.

plumes sporadically exist in the porous media. The convective transport of the plumes is likely hindered by the local weak velocity fields, so that local diffusive spreading dominates. The occurrence of the breakthrough curve tailing is favorable evidence for the non-Fickian behavior proposed by Dentz *et al.* [57], characterized by the diffusion of tracer paticles into immobile zones. To facilitate this analysis, we plotted the cross-sectional velocity distribution for the NaCl solution and tracer plumes (Fig. 10), with the velocity of the flow field weighted by the total fluid (solid lines) and the tracer particles (dashed lines with symbol) over the x (transverse) and y (longitudinal) planes.

Nissan and Berkowitz [58] indicated that for homogeneous porous media, the resemblance of the two curves demonstrates the ability of the tracer plume to sample the velocity field and hence the tendency of evolving toward an asymptotic state. The average velocity of the NaCl solution slightly fluctuates around the mean value in the longitudinal (within 23%) and transverse directions (∼1 mm/s), reflecting the relatively homogeneous nature of the pore structure and the

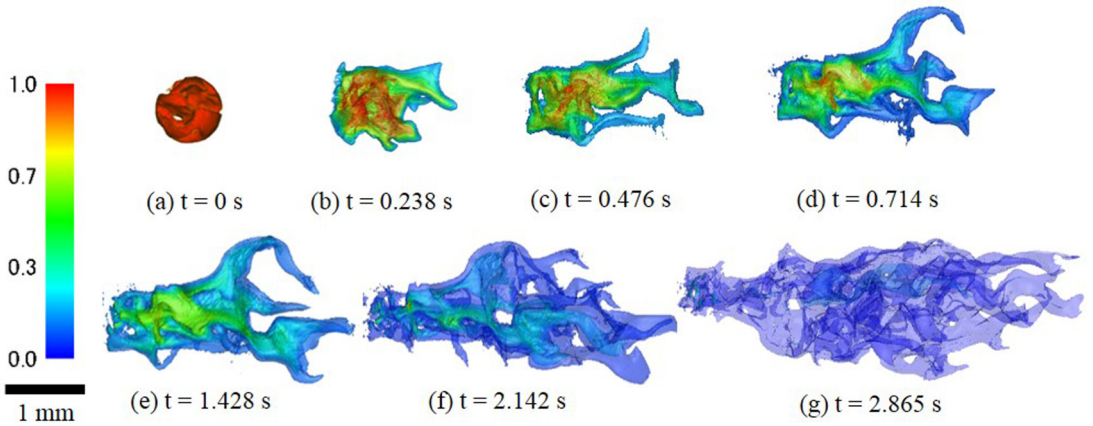

FIG. 8. Temporal evolution of the NaI tracer plume concentration profiles from LBM simulations. The time shown at the bottom of each profile is the transformed physical time. The initial shape of the tracer plume is spherical and occupies the space of around four particles. The colors denote isosurfaces of the solute concentration. The outer surface threshold is 6.25% of the initial concentration (Pe = 350.4, $d_p = 338\,\mu$m).

resulting flow field. In the transverse direction, the tracer velocity pattern resembles that of the NaCl solution. However, high velocities (nearly twice the mean value) are presented downstream of the flow in the longitudinal direction, whereas tails of the low-velocity zones exist near the initial centroid. This indicates the dominant effect of convective flow on the longitudinal dispersion at intermediate times, confirming the existing of preferential flow paths when diffusion fails to attenuate the tracer plume through stretching and tilting. In agreement with previous studies, some trapped tracer particles are present in the upstream flow path where the average tracer velocity is extremely slow, demonstrating the existence of immobile zones with heavy tails of low-concentration fields [59–61]. Furthermore, this trend persisted even after further transport of the plume. This finding implies trapping of the tracer particles in the stagnant zones, where local dispersivity and diffusion are important, and hence asymptotic dipsersion is attained after a long time. This analysis is consistent with the asssumption that the asymptotic dispersion behavior can possibly emerge after the localized concentration gradients of the interparticle pore throats are smoothened by diffusion [12,29].

C. MSD and LVCF

The MSD in the longitudinal direction exhibits ballistic scaling at early computational times with $\sigma_L^2 \sim t^2$, characteristic of perfectly correlated stratified flows [62,63]. By contrast, the dispersion in the transverse direction significantly varies before the ballistic region, especially for $\mathrm{Pe}_s > 58.4$ when unexpected negative values of the dispersion coefficient are encountered. A possible explanation is that convective flow and the underlying biased velocity field (preferential flow path) dominate the transverse dispersion for relatively high Pe. Therefore, the incomplete lateral mixing is associated with the localized flow field [60]. However, as mixing and diffusion of the tracer continue across streamlines, the localized effect is shortly eliminated, followed by the appearance of the ballistic region. For the sake of consistency, we plotted the MSD as a function of the rescaled time t/τ [Figs. 11(c) and 11(d)], representing the number of particles transported by convection at a given time t. The results show that the MSD in the longitudinal direction almost overlaps through the range of Pe, whereas some variations occur in the transverse direction where the MSD is higher for lower Pe. This finding indicates the strong effects of the convective flow on the longitudinal

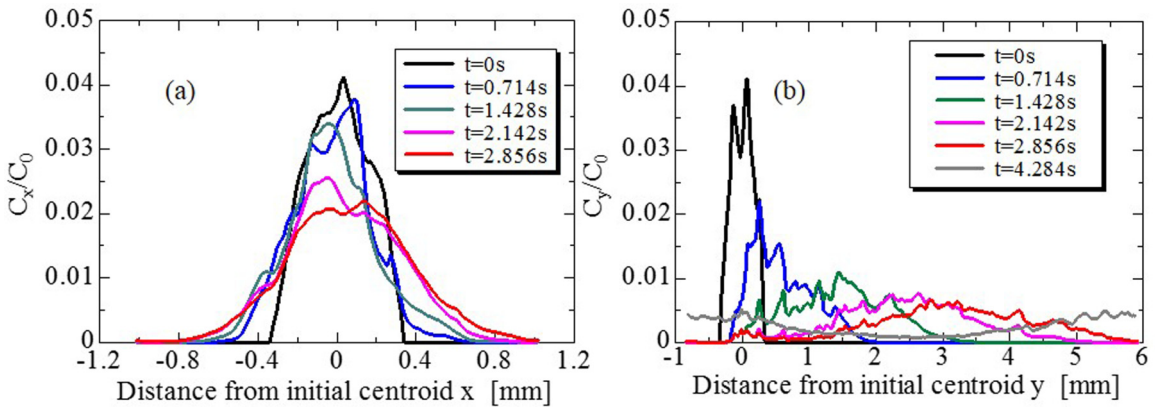

FIG. 9. Temporal evolution of the transverse (a) and longitudinal (b) tracer concentration. (Pe = 350.4, $d_p = 338\,\mu$m).

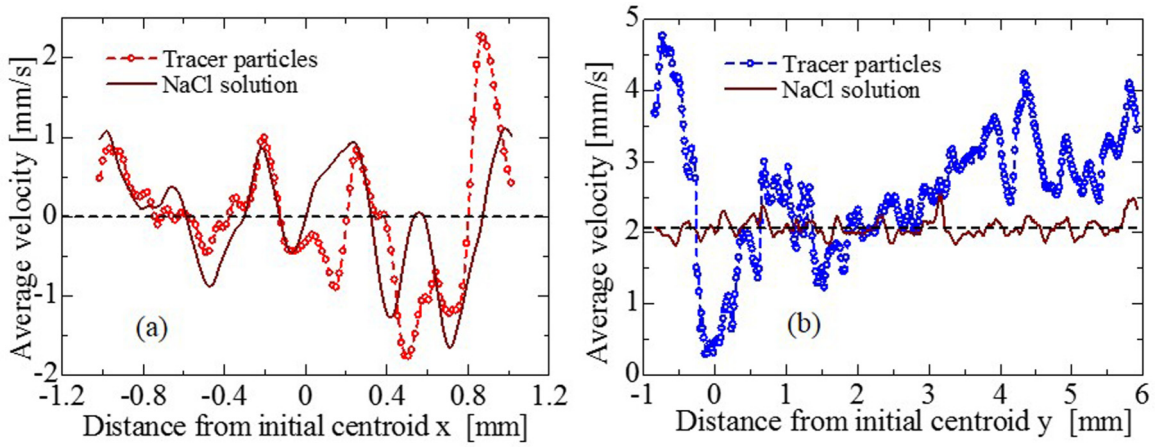

FIG. 10. Average velocity of the tracer particles and NaCl solution over the x and y planes. (Pe = 350.4, $d_p = 338\,\mu$m, t = 2.856 s). The dotted lines with open circles represent the average velocity of the tracer particles: (a) refers to the transverse direction and (b) refers to the longitudinal direction. The solid lines denote the average flow velocity with its statistical average expressed as the black dashed lines.

dispersion and the dependence of the transverse dispersion on physical diffusion, where lower Pe demands longer physical times for transport over the same length. Furthermore, no strict difference is apparent between the longitudinal and transverse directions for the MSD in the ballistic region, consolidating our understanding that this region mainly arises from the molecular diffusion across streamlines [10].

Following the ballistic dispersion region, a superdiffusive region is observed with $\sigma^2_{L,T} \sim t^n$, with n varying between 1 and 2. Despite the rapidity (approximately 8τ) in leaving the

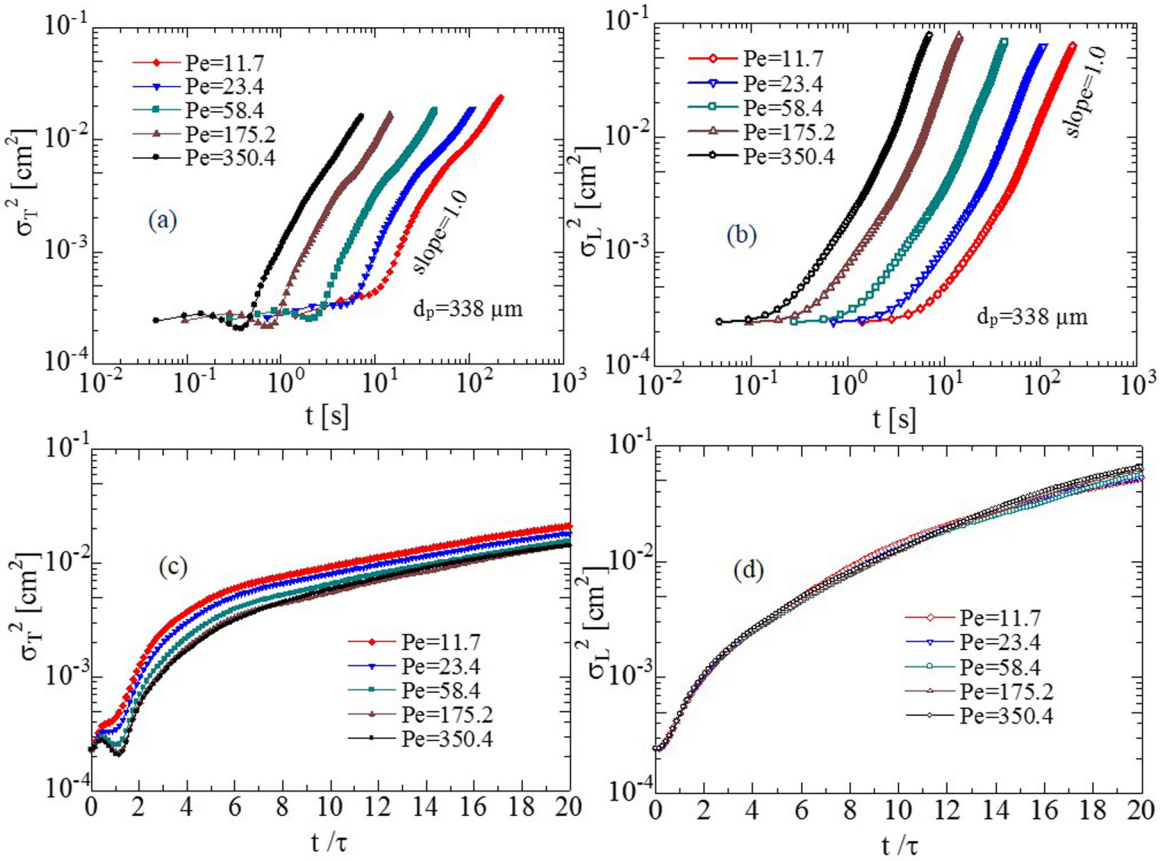

FIG. 11. MSD for LBM simulations. The total simulation times for Pe = 11.7, 23.4, 58.4, 175.2, and 350.4 are 214.2, 107.1, 42.84, 14.28, and 7.14 s, respectively. The closed-symbol dotted lines show the MSD in the transverse direction (a), whereas the open-symbol dotted lines represent that in the longitudinal direction (b). (c),(d) plot MSD with the rescaled time t/τ, where $\tau = d_p/u_{\mathrm{av}}$ is the characteristic convective time required for the tracer particle to transport a characteristic length L (in our study $L = d_p$).

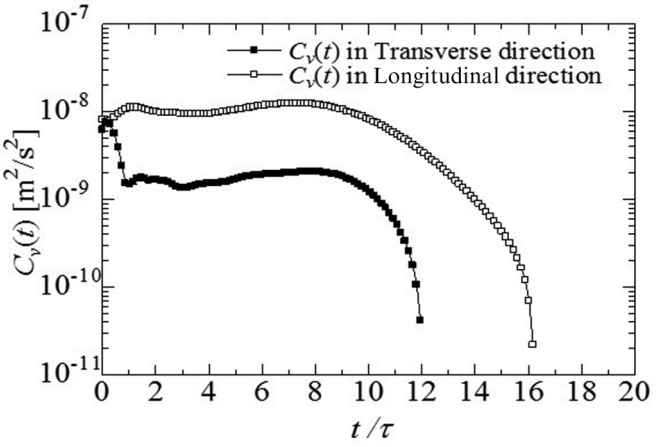

FIG. 12. LVCF (Pe = 350.4, $d_p = 338\,\mu$m). τ is characteristic time as previously specified. The filled squares represent the LVCF in the transverse direction, and the open squares denote the longitudinal direction.

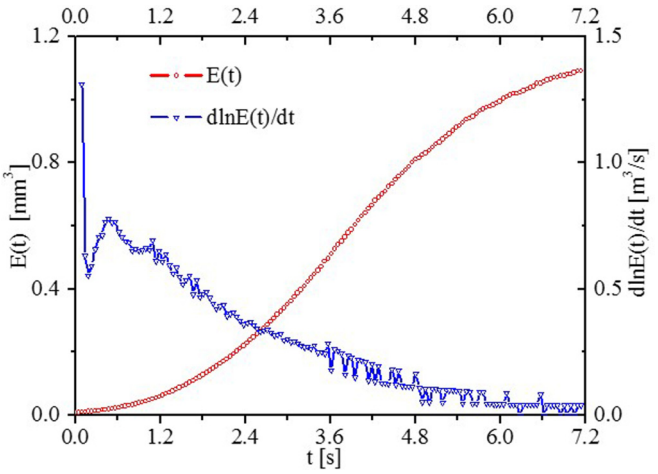

FIG. 13. Evolution of the dilution index $E(t)$ and temporal derivative of $\ln E(t)$.

ballistic region, the termination of this region is relatively hard to predict because of the persistent weak temporal dependence of the dispersion coefficients. To predict the dispersivity and assess the extent of the transient behavior, the LVCF [21] was calculated using Eq. (23):

$$C_v(t) = \langle [\boldsymbol{v}(0) - \bar{\boldsymbol{v}}] \cdot [\boldsymbol{v}(\boldsymbol{r}) - \bar{\boldsymbol{v}}] \rangle, \tag{23}$$

where $C_v(t)$ is the covariance of the velocity field at time t, $\boldsymbol{v}(\boldsymbol{r})$ is the tracer velocity along the flow direction at position $\boldsymbol{r} = \bar{\boldsymbol{v}}t$, and $\bar{\boldsymbol{v}}$ is the average flow velocity. The angular brackets represent the average over the whole domain.

$C_v(t)$ represents disorder-induced velocity perturbations over large distances, which decayed exponentially and converged to zero at the characteristic time for asymptotic dispersion [21].

From the Green-Kubo relations and Einstein's definition of diffusion coefficient D [15], we can relate the LVCF with the MSD by using Eq. (24).

$$D = \lim_{t\to\infty} \frac{d\delta^2(t)}{2dt} = \int_0^\infty C_v(t')dt'. \tag{24}$$

From Fig. 12, the effect of the initial tracer configuration is hardly visible after the convective time of 1τ, beyond which a plateau is observed in the transverse and longitudinal directions until 8τ. The existence of the plateau is possibly a straightforward reflection of the ballistic dispersion regime. $C_v(t)$ exponentially decayed with time toward an infinitesimal value, reaching the preasymptotic dispersion. The fact that $C_v(t)$ decays much faster in the transverse direction than in the longitudinal direction implies that the transverse dispersion reaches the asymptotic region much faster. This result is consistent with the result from the MSD [refer to Figs. 11(c) and 11(d)] and is in agreement with Howington *et al.* [15], who studied the transient dispersion behaviors in unconfined monosized sphere packings. These authors suggested that the longer transverse transient time is likely originated from convection-induced transverse displacement surrounding the spheres. Furthermore, in our simulation, the rescaled preasymptotic time for the transverse and longitudinal directions is 12 and 16 convective times, respectively, whereas for the dispersion in the homogeneous random sphere packing, the time is approximated to between 5 and 10 convective times [15]. This finding suggests that asymptotic dispersion is attainable on several convective timescales, although many heterogeneous porous structures like those in this study require longer transient times then the spherical ones.

D. Dilution index

The dilution index $E(t)$ is a parameter proposed by Kitanidis [64] to quantify the dilution and mixing state of a passive tracer. It was experimentally [5] and theoretically [65] adopted to represent tracer concentration distributions within a plume in heterogeneous porous media. This index is defined as

$$E(t) = \exp\left(-\int p(\mathbf{r},t)\ln[p(\mathbf{r},t)]dV\right), \tag{25}$$

where $p(\mathbf{r},t)$ is the local normalized tracer concentration, such that $p(\mathbf{r},t) = C(\mathbf{r},t)/\sum_{\mathbf{r}} C(\mathbf{r},t)$. It has the unit of volume in the 3D domain. Plausibly, advection creates no volume change, but deformation has no direct impact on it. Thus, this quantity can stochastically indicate the mixing state of the dispersion system and is representative of the gross dispersivity [64]. The analytical solution for the dilution index equation for an instantaneous release of a plume with Gaussian distribution is provided by Barros *et al.* [66]. The dilution index at early times exhibits a power law relationship with time presented as $E(t) \sim t^{n/2}$, with n as the dimension of the domain. In our study, the power law is estimated as 1.39 for early times and $E(t)$ is almost stabilized at relatively later times. Furthermore, the logarithm of the index is a familiar expression for "entropy." With the constant deformation of the irregular plume shape in the heterogeneous porous media, $\ln E(t)$ monotonously increases, but its temporal derivative unbiasedly decreases to nearly zero, indicative of the convergence of the dispersion coefficients (Fig. 13).

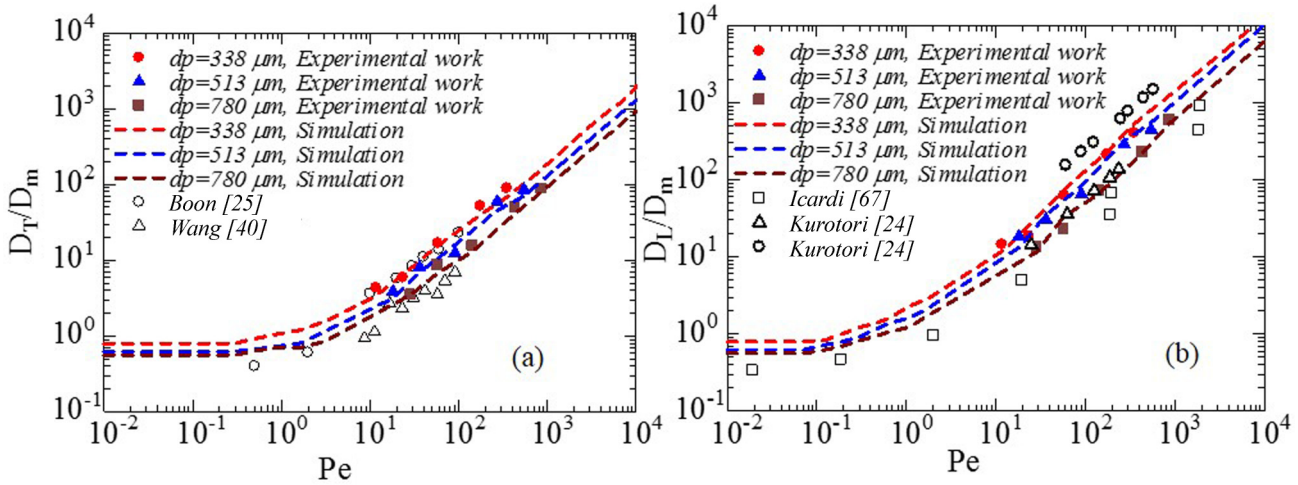

FIG. 14. Dependence of the normalized dispersion coefficients ($D_{T/L}/D_m$) on Pe. The filled symbols represent the current experimental results (red circles, blue triangles, and brown squares are for the mean particle diameters d_p of 338, 513, and 780 μm, respectively). The dashed lines correspond to the fitted curves from the present LBM and MPM simulations. The open symbols denote the dispersion data from previous studies. In (a), the open circles represent the results for the Berea sandstones [25], whereas the open triangles represent the same porous media but with larger sizes [40]. In (b), the open squares are associated with the CFD simulation results for confined sand packing [67], whereas the open circles and triangles are for the experimental results of the Ketton limestone and packed beads [24].

E. Dispersion coefficient

As suggested by Sahimi [23], dispersion in disordered porous media undergoes the diffusive regime at Pe $\ll 1$ and then the power-law regime (also called the boundary-layer dispersion regime) at $5 < \mathrm{Pe} < 300$, with the dominance of convective flow over dispersion, without neglecting the effect of diffusion. The mechanical dispersion regime is discovered at $300 < \mathrm{Pe} < 10^5$, which is generated by the stochastic velocity variations. The numerical descriptions of these regimes are as follows:

$$\mathrm{Pe} \ll 1, \quad \frac{D_{L,t}}{D_m} = \frac{1}{\mathrm{F}\phi}, \tag{26}$$

$$5 < \mathrm{Pe} < 300, \quad \frac{D_{L,t}}{D_m} = \beta_{L,T}\mathrm{Pe}^{\delta_{L,T}}, \tag{27}$$

$$300 < \mathrm{Pe} < 10^5, \quad \frac{D_{L,t}}{D_m} = \alpha_{L,T}\mathrm{Pe}. \tag{28}$$

In the above equation; F is the formation factor, ϕ is porosity; α, β, and δ are the fitted coefficients; and the power law with the subscript L/T corresponds to the focused direction. Besides the experiments, our simulation work samples a wide range of $10^{-2} < \mathrm{Pe} < 10^4$ to confidently fit the curves. The transverse and longitudinal dispersion coefficients are acquired from the method of moments and plotted as a function of Pe in Fig. 14. The results from our study (filled symbols for experiments and dashed lines for simulation) are qualitatively compared with the existing results for sandstones and packed particle beads (open symbols) from different previous studies. However, most of the curves fall in the same range, and the estimated dispersion coefficients are much lower than those of the more heterogeneous sandstones (open circle) and slightly higher than those of the packed particles (open triangle and square).

The simulation results (dashed lines) accurately capture the experimental dispersion behaviors in the power-law regime. As suggested, a power-law dependence of the dispersion coefficient on the Pe [23] mainly originates from the existence of stagnation zones ([12]; diffusive boundary layers) characterized by intraparticle fluid retention regions [68] and relatively low diffusivity. The fitted parameters are presented in Table III, with subdiffusive behaviors in the transverse direction showing $\delta_T \sim 0.95$, whereas superdiffusive behaviors are in the longitudinal direction with $\delta_L \sim 1.1$. These results are coherent with the correlations quantified by Sahimi [23], in which δ_T and δ_L are estimated as $\delta_T \sim 0.9$ and $\delta_L \sim 1.2$, respectively. For the diffusive regime, the formation factor is estimated by placing the tracer plume in motionless NaCl solutions. The tortuosity of the porous media estimated with $\gamma = F\phi$ falls in a range of 1.12–1.76, which is a reasonable approximation for our porous structures. The threshold Pe for this regime is almost 1 in the transverse direction and 0.1 in

TABLE III. Fitted dispersion parameters from experiments and simulations.

	Experiment				Simulation						
d_p (μm)	β_T	δ_T	β_L	δ_L	β_T	δ_T	β_L	δ_L	F	α_T	α_L
338	0.35	0.96	0.92	1.04	0.36	0.91	0.84	1.10	2.25	0.19	1.38
513	0.55	0.94	0.97	0.99	0.24	0.92	0.60	1.09	3.28	0.13	1.01
780	0.46	0.93	0.57	1.12	0.16	0.92	0.34	1.09	3.78	0.09	0.62

the longitudinal direction. The mechanical dispersion regime is achieved at a relatively higher Pe with linear dependence of the dispersion coefficients; however, the longitudinal dispersion coefficient is 6 or 7 times higher than its transverse counterpart as indicated by the value of $\alpha_{L,T}$ in Table III.

VI. CONCLUSIONS

We investigated the dispersion behaviors of a nonreactive NaI plume in a randomly packed bed of unconsolidated melamine resin particles using micro-CT. The dispersion process was visualized and vastly quantified in a Pe range from 11.7 to ∼860. The result suggested that the asymptotic dispersion region is obtained for all experiments. We then performed pore-scale simulations to compare the experimental results and elucidate the associated dispersion mechanisms. The LBM with He's forcing scheme was utilized to simulate the flow field, whereas the MPM was adopted for the simulation of the evolution of the tracer plume (dispersion process). The computational scheme was validated against the theory of shear-induced Taylor dispersion in a tube.

The results demonstrate that the dispersion behaviors in the simulation and experiments exhibit similar patterns. The sporadically isolated tracer clouds are discovered at the upstream of dispersion and can be further explained by the associated velocity structures characterized with the stagnation zones and preferential flow paths. The asymptotic dispersion is obtainable after the tracer particles have sampled the velocity fields. The pore-scale dispersion simulation revealed ballistic and superdiffusive regimes at the transient times, whereas standard asymptotic dispersion behaviors emerged at longer characteristic times. The initial distribution of the tracer plume showed a negligible effect on dispersion. Then, the transient period is directly recognized by the LVCF function and is persistent over length scales of approximately 12 and 16 particles for the transverse and longitudinal directions, respectively. The obtainment of the asymptotic dispersion is consolidated by analyzing through the method of moment and dilution index, which shows linear growth of the mean-square displacement and the decrease of the temporal derivative of $\ln E(t)$ to infinitesimal.

Most of the dispersion experiments fell in the power-law regime ($50 < \mathrm{Pe} < 300$), where the dispersion process is dominated by convection, whereas the effect of diffusion cannot be ignored. In this regime, the estimated dispersion coefficients from our simulation show robust consistency with the experimental work and previous publications. The subdiffusive and superdiffusive behaviors are recognized with a power-law dependence of the dispersion coefficient on the Pe following $\delta_T \sim 0.95$ and $\delta_L \sim 1.1$. These results are coherent with the correlations quantified by Sahimi [23] with $\delta_T \sim 0.9$ and $\delta_L \sim 1.2$. Apart from this regime, the diffusive regime at $\mathrm{Pe} \ll 1$ and the mechanical dispersion regime at $300 < \mathrm{Pe} < 10^5$ are recognized through simulations. The threshold Pe for the diffusive regime is 1 in the transverse direction and 0.1 in the longitudinal direction. The tortuosity of the porous media estimated from $\gamma = F\phi$ falls between 1.12 and 1.76. The mechanical dispersion regime is achieved at a relatively higher Pe, with a linear dependence of the dispersion coefficients on Pe. In this regime, the coefficients in the longitudinal direction are 6–7 times higher than those in the transverse direction.

ACKNOWLEDGMENTS

This work was supported by JSPS KAKENHI with Grant No. 17H00790. The authors also greatly appreciate the endowment of the Tsubame Scholarship from Tokyo Institute of Technology.

[1] A. Xu, W. Shyy, and T. Zhao, Acta Mech. Sin. **33**, 555 (2017).
[2] B. Berkowitz, I. Dror, and B. Yaron, *Contaminant Geochemistry*, 2nd ed. (Springer, Berlin, 2014).
[3] R. Alonso-Matilla, B. Chakrabarti, and D. Saintillan, Phys. Rev. Fluids **4**, 043101 (2018).
[4] M. Sahimi, Phys. Rev. E **85**, 016316 (2012).
[5] M. Moroni, N. Kleinfelter, and J. H. Cushman, Adv. Water Resour. **30**, 1 (2007).
[6] B. Bijeljic, P. Mostaghimi, and M. J. Blunt, Water Resour. Res. **49**, 2714 (2013).
[7] D. W. Meyer and B. Bijeljic, Phys. Rev. E **94**, 013107 (2016).
[8] A. Comolli, J. J. Hidalgo, C. Moussey, and M. Dentz, Transp. Porous Media **115**, 265 (2016).
[9] N. B. Engdahl, T. R. Ginn, and G. E. Fogg, J. Contam. Hydrol. **149**, 46 (2013).
[10] C. E. Naylor, S. Gover, A. K. Basak, M. S. Cosgrove, H. R. Levy, and M. J. Adams, Acta Cryst. D **57**, 635 (2001).
[11] V. L. Morales, M. Dentz, M. Willmann, and M. Holzner, Geophys. Res. Lett. **44**, 9361 (2017).
[12] D. Kandhai, D. Hlushkou, A. G. Hoekstra, P. M. Sloot, H. Van As, and U. Tallarek, Phys. Rev. Lett. **88**, 234501 (2002).
[13] G. I. Taylor, Proc. Phys. Soc. London Sect. B **67**, 857 (1954).
[14] C. Bruderer and Y. Bernabé, Water Resour. Res. **37**, 897 (2001).
[15] S. E. Howington, R. S. Bernard, R. S. Maier, H. T. Davis, D. M. Kroll, and J. F. Peters, Phys. Fluids **15**, 3795 (2003).
[16] D. Maggiolo, F. Picano, and M. Guarnieri, Phys. Fluids **28**, 102001 (2016).
[17] P. K. Kang, P. de Anna, J. P. Nunes, B. Bijeljic, M. J. Blunt, and R. Juanes, Geophys. Res. Lett. **41**, 6184 (2014).
[18] M. Dentz, J. Carrera, and J.-R. de Dreuzy, Phys. Rev. E **84**, 019904 (2011).
[19] I. Ginzburg, Adv. Water Resour. **118**, 49 (2018).
[20] M. B. Cardenas, Geophys. Res. Lett. **35**, L08402 (2008).
[21] F. Capuani, D. Frenkel, and C. P. Lowe, Phys. Rev. E **67**, 056306 (2003).
[22] J. M. P. Q. Delgado, Heat Mass Transfer **42**, 279 (2006).
[23] M. Sahimi, Rev. Mod. Phys. **65**, 1393 (1993).
[24] T. Kurotori, C. Zahasky, S. A. Hosseinzadeh Hejazi, S. M. Shah, S. M. Benson, and R. Pini, Chem. Eng. Sci. **196**, 366 (2019).
[25] M. Boon, B. Bijeljic, B. Niu, and S. Krevor, Adv. Water Resour. **96**, 266 (2016).
[26] T. Ritschel, S. Schlüter, J. M. Köhne, H. J. Vogel, and K. U. Totsche, Water Resour. Res. **54**, 9033 (2018).

[27] V. Clausnitzer and J. W. Hopmans, Water Resour. Res. **36**, 2067 (2000).
[28] H. M. D. Agbogun, T. A. Al, and E. M. A. Hussein, J. Contam. Hydrol. **145**, 44 (2013).
[29] M. Boon, B. Bijeljic, and S. Krevor, Water Resour. Res. **53**, 4624 (2017).
[30] X. Yang, Y. Mehmani, W. A. Perkins, A. Pasquali, M. Schönherr, K. Kim, M. Perego, M. L. Parks, N. Trask, M. T. Balhoff, M. C. Richmond, M. Geier, M. Krafczyk, L.-S. Luo, A. M. Tartakovsky, and T. D. Scheibe, Adv. Water Resour. **95**, 176 (2016).
[31] S. Chen and G. D. Doolen, Annu. Rev. Fluid Mech. **30**, 329 (1998).
[32] S. Succi, *The Lattice Boltzmann Equation* (Oxford University Press, Oxford, 2018).
[33] C. P. Lowe and D. Frenkel, Phys. A (Amsterdam, Neth.) **220**, 251 (1995).
[34] R. M. H. Merks, A. G. Hoekstra, and P. M. A. Sloot, J. Comput. Phys. **183**, 563 (2002).
[35] D. Yu, S. S. Girimaji, and A. J. C. Ladd, Phys. Rev. E **78**, 056706 (2008).
[36] B. Rotenberg, I. Pagonabarraga, and D. Frenkel, Europhys. Lett. **83**, 34004 (2008).
[37] J. Vanson, F.-X. Coudert, M. Klotz, and A. Boutin, Langmuir **33**, 1405 (2017).
[38] A. Asta, M. Levesque, and B. Rotenberg, Mol. Phys. **116**, 2965 (2018).
[39] S. Sin, T. Suekane, Y. Nagatsu, and A. Patmonoaji, Phys. Rev. Fluids **4**, 054502 (2019).
[40] L. Wang, Y. Nakanishi, A. Hyodo, and T. Suekane, Int. J. Greenhouse Gas Control **53**, 274 (2016).
[41] J. H. Wang and J. W. Kennedy, J. Am. Chem. Soc. **72**, 2080 (1950).
[42] X. He and L.-S. Luo, Phys. Rev. E **56**, 6811 (1997).
[43] A. A. Mohamad, *Lattice Boltzmann Method*, 1st ed. (Springer, London, 2011).
[44] X. He, S. Chen, and G. D. Doolen, J. Comput. Phys. **146**, 282 (1998).
[45] M. Sbragaglia, R. Benzi, L. Biferale, S. Succi, K. Sugiyama, and F. Toschi, Phys. Rev. E **75**, 026702 (2007).
[46] H. Huang, M. Krafczyk, and X. Lu, Phys. Rev. E **84**, 046710 (2011).
[47] Z. Guo, C. Zheng, and B. Shi, Phys. Rev. E **65**, 046308 (2002).
[48] B. Servan-Camas and F. T. C. Tsai, J. Comput. Phys. **228**, 236 (2009).
[49] N. S. Bakhvalov, in *Encyclopedia of Mathematics*, edited by Michiel Hazewinkel (Springer, Berlin, 2001).
[50] R. Courant, K. Friedrichs, and H. Lewy, Math. Ann. **100**, 32 (1928).
[51] G. A. Gist, A. H. Thompson, A. J. Katz, and R. L. Higgins, Phys. Fluids A **2**, 1533 (1990).
[52] F. De Smedt, W. Brevis, and P. Debels, J. Hydrol. **315**, 25 (2005).
[53] W. R. Young and S. Jones, Phys. Fluids A **3**, 1087 (1991).
[54] H. Brenner, Philos. Trans. R. Soc., A **297**, 81 (1980).
[55] Y. Nakanishi, A. Hyodo, L. Wang, and T. Suekane, Adv. Water Resour. **97**, 224 (2016).
[56] D. Bolster, M. Dentz, and T. Le Borgne, Water Resour. Res. **47**, 1 (2011).
[57] M. Dentz, M. Icardi, and J. J. Hidalgo, J. Fluid Mech. **841**, 851 (2018).
[58] A. Nissan and B. Berkowitz, Phys. Rev. E **99**, 033108 (2019).
[59] I. L. Molnar, J. I. Gerhard, C. S. Willson, and D. M. O'Carroll, Water Resour. Res. **51**, 8973 (2015).
[60] T. D. Scheibe, Z. Hou, B. J. Palmer, and A. M. Tartakovsky, Water Resour. Res. **49**, 4277 (2013).
[61] R. Aziz, V. Joekar-Niasar, and P. Martinez-Ferrer, Int. J. Multiphase Flow **109**, 51 (2018).
[62] M. Holzner, V. L. Morales, M. Willmann, and M. Dentz, Phys. Rev. E **92**, 013015 (2015).
[63] A. Puyguiraud, P. Gouze, and M. Dentz, Transp. Porous Media **128**, 837 (2019).
[64] P. K. Kitanidis, Water Resour. Res. **30**, 2011 (1994).
[65] F. P. J. De Barros, M. Dentz, J. Koch, and W. Nowak, Geophys. Res. Lett. **39**, 1 (2012).
[66] F. P. J. De Barros, A. Fiori, F. Boso, and A. Bellin, J. Contam. Hydrol. **175–176**, 72 (2015).
[67] M. Icardi, G. Boccardo, D. L. Marchisio, T. Tosco, and R. Sethi, Phys. Rev. E **90**, 013032 (2014).
[68] U. Tallarek, F. J. Vergeldt, and H. Van As, J. Phys. Chem. B **103**, 7654 (1999).